Atmos. Chem. Phys. Discuss., https://doi.org/10.5194/acp-2017-839
Manuscript under review for journal Atmos. Chem. Phys.
Discussion started: 13 November 2017

Atmospheric Chemistry and Physics
Discussions

Subgrid-scale variability of clear-sky relative humidity and forcing by aerosol-radiation interactions in an atmosphere model

Paul Petersik[1], Marc Salzmann[1], Jan Kretzschmar[1], Ribu Cherian[1], Daniel Mewes[1], and Johannes Quaas[1]
[1]Leipzig Institute for Meteorology, Universität Leipzig
Correspondence to: Paul Petersik (paul.j.petersik@gmail.com)

Abstract. Atmosphere models with resolutions of several tens of kilometres take subgrid-scale variability of the total specific humidity q_t into account by using a uniform probability density function (PDF) to predict fractional cloud cover. However, usually only mean relative humidity $\overline{\mathrm{RH}}$ or mean clear-sky relative humidity $\overline{\mathrm{RH}}_{\mathrm{cls}}$ is used to compute hygroscopic growth of soluble aerosol particles. In this study, a stochastic parameterization of subgrid-scale variability of $\mathrm{RH}_{\mathrm{cls}}$ is applied. For this, we sample the subsaturated part of the uniform RH-PDF from the cloud cover scheme for application in association with the hygroscopic growth parameterization in the ECHAM6-HAM2 atmosphere model. Due to the non-linear dependence of the hygroscopic growth on RH, this causes an increase in aerosol hygroscopic growth. Aerosol optical depth (AOD) increases by a global mean of 0.009 ($\sim 7.8\,\%$ in comparison to the control run). Especially over the tropics AOD is enhanced with a mean of about 0.013. The ability of the model to simulate AOD is slightly improved with respect to satellite data from MODIS-Aqua. Due to the increase in AOD, net top of the atmosphere clear-sky solar radiation decreases by $-0.22\,\mathrm{W\,m^{-2}}$ ($\sim -0.08\,\%$). Finally, the effective radiative forcing due to aerosol-radiation interactions under clear-sky conditions ($\mathrm{ERFari_{cls}}$) changes from $-0.29\,\mathrm{W\,m^{-2}}$ to $-0.45\,\mathrm{W\,m^{-2}}$ by about 57 %. The reason for this very disproportionate effect is that anthropogenic aerosols are disproportionally hygroscopic.

1 Introduction

Aerosols have a significant impact on the climate system by interacting with radiation and clouds. Solar and thermal radiation interact with aerosols by absorption and scattering processes. Despite extensive research on atmospheric aerosols, the effective radiative forcing due to aerosol-radiation interactions (ERFari) has still a large uncertainty. The ERFari combines effects from radiative forcing due to aerosol-radiation interactions (RFari) and rapid adjustments and is estimated to be -0.45 (-0.95 to $+0.05$) $\mathrm{W\,m^{-2}}$ by the 5th assessment report (AR5) of the Intergovernmental Panel on Climate Change (IPCC) (Boucher et al., 2013). The radiative forcing by aerosol-radiation interactions from sulphate ($-0.4\,\mathrm{W\,m^{-2}}$) and nitrate ($-0.11\,\mathrm{W\,m^{-2}}$) is a cooling effect on the radiative balance of the Earth due to increased scattering of solar radiation. In contrast, black carbon ($+0.4\,\mathrm{W\,m^{-2}}$) is warming the Earth's climate due to absorption of solar radiation. Additionally, it is uncertain if primary and secondary organic aerosols, aerosols from biomass burning and mineral dust have a net cooling or a warming effect (Ginoux, 2017). In total, anthropogenic aerosols have very likely a cooling effect through aerosol-radiation interactions on the radiative balance of the Earth (Boucher et al., 2013).

Through various non-linear relationships described by Beer-Lambert's law (Lambert, 1760; Beer, 1852) and Mie scattering (Mie, 1908), the extinction of radiation is related to the aerosol particle radius. The aerosol particle radius of hygroscopic aerosols like sulphate or sea salt aerosols increases in a humid environment due to attraction of water. This hygroscopic growth is a non-linear function of the ambient relative humidity (RH), where hygroscopic growth is especially enhanced close to saturation (Köhler, 1936). Therefore, extinction due to hygroscopic aerosols increases strongly when the humidity of the ambient air approaches saturation (Zieger et al., 2013; Skupin et al., 2016; Haarig et al., 2017).

However, it is known that humidity varies on subgrid scales in global circulation models with largest subgrid-scale variability in the middle troposphere (Quaas, 2012). General circulation models (GCMs) that just use the grid-box mean relative humidity $\overline{\mathrm{RH}}$ to calculate hygroscopic growth of aerosols do not take this subgrid-scale variability of humidity and its effect on radiation into account. Various studies show that GCMs underestimate the RFari of sulphate aerosols by 30 to 80 % when not considering subgrid-scale variability of RH for the hygroscopic growth of sulphate particles (Haywood et al., 1997; Petch, 2001; Myhre et al., 2002). In addition, recent studies show that models with a coarse resolution which do not take subgrid-scale variability of various aerosol properties into account underestimate aerosol radiative forcing (Gustafson et al., 2011) and have a significant negative bias in aerosol optical depth (Weigum et al., 2016). The mentioned studies use high resolution models and compare the results from calculations of radiative forcing that keep the high resolution of RH with either calculation where RH is averaged spatially beforehand to mimic a GCM resolution or results from model configurations with a coarser resolution.

Haywood and Shine (1997) and Haywood and Ramaswamy (1998) include subgrid-scale variability of RH for the calculation of RFari by sulphate directly into GCM simulations. Haywood and Shine (1997) prescribe the RH distribution globally for clear skies. Here, for each grid cell and height level five fixed RH-values are taken from a normal distribution around RH= 70 %. They find that RFari by sulphate is 24% greater than the non-hydrated forcing when using the grid-box mean RH. However, RFari by sulphate increases up to 37% when the subgrid-scale variability of RH is applied and the correlation between clouds and areas of high relative humidity is taken into account. Hence, RFari by sulphate increased by about 10% from simulations that use grid-box mean RH to simulations with a subgrid-scale variability of RH. Haywood and Ramaswamy (1998) have a more sophisticated approach. They use a triangular shaped relative humidity distribution around the grid-box mean RH with a magnitude of ±10% that is truncated at RH=1.0 as proposed by Haywood et al. (1997). However, the authors emphasize that they do not consider variations of width and shape of the used distribution. In their study RFari by sulphate is enhanced by 9% due to the subgrid-scale variability of RH when including clouds.

In this study, we implement a stochastic parameterization of subgrid-scale variability of clear-sky relative humidity $\mathrm{RH}_{\mathrm{cls}}$ into the global aerosol-climate model of the Max Planck Institute for Meteorology (MPI-M) ECHAM6-HAM2 (Zhang et al., 2012). For this, we use a uniform probability density function (PDF) that reproduces the subsaturated part of the cloud cover scheme from Sundqvist et al. (1989) that is used by ECHAM6 (Stevens et al., 2013). The width of the PDF from the cloud cover scheme is a function of height. Hence, our parameterization inherits this feature. ECHAM6-HAM2 until now used the grid box-mean clear-sky relative humidity $\overline{\mathrm{RH}}_{\mathrm{cls}}$ in the cloud free part of the model to calculate hygroscopic growth (Zhang et al., 2012). $\overline{\mathrm{RH}}_{\mathrm{cls}}$ is chosen, instead of grid-box mean relative humidity $\overline{\mathrm{RH}}$, because cloud processing and cloud radiative effects are dominant in the cloudy part of a grid box. That means, aerosol-radiation interactions are negligible in the cloud part. Now, rather than using the grid-box mean, the PDF of the subgrid-scale variability of $\mathrm{RH_{cls}}$ is randomly sampled for each time step, grid cell and height level to compute the growth factor gf (see section 2). Hygroscopic growth is computed in ECHAM6-HAM2 for all hygroscopic aerosol constituents that are incorporated in the model. Therefore, the effect subgrid-scale variability of $\mathrm{RH_{cls}}$ on hygroscopic growth is included for all hygroscopic aerosol particles in the model. In section 3 we investigate how the new parameterization changes optical and radiative properties of the atmosphere. Afterwards, the results are discussed in section 4. Finally, this study is summarized with an outlook for further research in section 5.

2 Methods

2.1 Hygroscopic growth in ECHAM6-HAM2

Hygroscopic growth can be described by the growth factor $gf = r_{\mathrm{wet}}/r_{\mathrm{dry}}$, where r_{wet} and r_{dry} are the wet and dry radius of an aerosol particle, respectively. Petters and Kreidenweis (2007) introduced the κ-Köhler theory to calculate the growth factor as a function of relative humidity and temperature

$$\frac{\mathrm{RH}}{\exp\left(\frac{A_{\mathrm{K}}(T)}{D_{\mathrm{dry}}\,gf}\right)} = \frac{gf^3 - 1}{gf^3 - (1-\kappa)} \tag{1}$$

where RH is the ambient relative humidity, D_{dry} the dry diameter, A_{K} the temperature-dependent parameter of the Kelvin (curvature) effect and κ the hygroscopicity. A κ value of 0 describes completely hydrophobic aerosols, whereas κ values greater than 0.5 describe very hygroscopic aerosols. Common aerosol constituents with high κ values are sulphate (0.33 - 0.72), nitrate (~ 0.8) and sea spray (0.91 - 1.33) (Zhang et al., 2012). In Eq. (1) gf is a strictly-monotonically increasing, non-linear function with positive curvature for $\mathrm{RH} \in [0,1]$.

ECHAM6-HAM2 uses the grid-box mean clear-sky relative humidity $\overline{\mathrm{RH}}_{\mathrm{cls}}$ in Eq. (1). $\overline{\mathrm{RH}}_{\mathrm{cls}}$ is diagnosed from predicted $\overline{\mathrm{RH}}$. For this, saturation is assumed in clouds ($\mathrm{RH} = 1$). When the grid-box is cloud-free ($f = 0$) or partly cloudy ($0 < f < 1$), clear-sky relative humidity is computed by $\overline{\mathrm{RH}}_{\mathrm{cls}} = \left(\overline{\mathrm{RH}} - f\right)/(1-f)$ where f is the fractional cloud cover. For overcast grid-boxes ($f = 1$), the clear-sky relative humidity is not defined and set to saturation as well ($\overline{\mathrm{RH}}_{\mathrm{cls}} = 1$). Using the $\overline{\mathrm{RH}}_{\mathrm{cls}}$ in Eq. (1) implies that no subgrid-scale variability of $\mathrm{RH_{cls}}$ is used beyond the information supplied by the fractional cloud cover.

The aerosol module HAM2 calculates hygroscopic growth for each aerosol mode. There are 7 log-normal (4 soluble (S) and 3 insoluble (I)) modes to describe the size distribution of atmospheric aerosol. The modes are divided into Nucleation (N, $r < 0.005\,\mu\mathrm{m}$), Aitken (K, $0.005 < r < 0.05\,\mu\mathrm{m}$), Accumulation (A, $0.05 < r < 0.5\,\mu\mathrm{m}$) and Coarse (C, $r > 0.5\,\mu\mathrm{m}$) mode and are abbreviated in the following such as CS for soluble Coarse mode. The main hygroscopic aerosol constituents are sea salt (SS), sulphate (SO4) and organic carbon (OC). Mineral dust (DU) and black carbon (BC) are considered as non-hygroscopic on emission but may age due to internal mixing.

In the ECHAM model, subgrid-scale variability of specific humidity is used for the prediction of fractional cloud cover (Stevens et al., 2013). The cloud scheme assumes a uniform probability density function (PDF) as proposed by Sundqvist et al. (1989) for the horizontal subgrid-scale variability of total-water q_t between $\bar{q}_\mathrm{t} - \Delta q$ and $\bar{q}_\mathrm{t} + \Delta q$, where $\Delta q = \gamma q_\mathrm{s}$ (see Fig. 1a). $\bar{q}_\mathrm{t}$ is the model-predicted grid-box mean total-water specific humidity and q_s the saturation specific humidity computed from the predicted grid-box mean temperature. The scaling parameter γ is varying in the vertical but otherwise assumed to be constant in space and time. It can be calculated by $\gamma = 1 - \mathrm{RH}_\mathrm{crit}$, where $\mathrm{RH}_\mathrm{crit}$ is the critical relative humidity (Quaas, 2012; Rosch et al., 2015). Fractional cloud cover occurs if the grid box mean relative humidity $\overline{\mathrm{RH}}$ exceeds the critical relative humidity. In ECHAM6-HAM2 $\mathrm{RH}_\mathrm{crit}$ is parametrized as a function of height

$$\mathrm{RH}_\mathrm{crit}(p) = c_\mathrm{t} + (c_\mathrm{s} - c_\mathrm{t})\exp\left[1 - \left(\frac{p_\mathrm{s}}{p}\right)^{n_\mathrm{x}}\right] \tag{2}$$

with p the ambient pressure and p_s the surface pressure and c_t and c_s the critical relative humidity values at the top of the atmosphere (TOA) and the surface, respectively.

While the formulation of $\mathrm{RH}_\mathrm{crit}$ is specific to the ECHAM6 model, the cloud cover scheme from Sundqvist et al. (1989) has also been applied in other global models. Furthermore, the Tiedtke (1993) cloud cover scheme which is for example used in the Geophysical Fluid Dynamics Laboratory (GFDL) atmosphere model AM3 (Donner et al., 2011) assumes a uniform PDF of total water as well. While several global atmosphere models including ECHAM6-HAM2 make assumptions to account for the subgrid-scale variability of vertical velocity when computing droplet activation rates (Ghan et al., 1997; Lohmann et al., 2007; Golaz et al., 2011), subgrid-scale variability of RH or RH_cls is usually not taken into account when computing hygroscopic growth of interstitial aerosols.

2.2 Stochastic parameterization for the subgrid-scale variability of clear-sky relative humidity

For the stochastic parameterization, we use the subsaturated part of the q_t-PDF from the cloud cover scheme in not-overcast cases (see Fig. 1a). This diagnosed PDF is transformed into a RH_cls-PDF dividing it by q_s. Afterwards, it is sampled for the stochastic parameterization of subgrid-scale variability of RH_cls. The width of the q_t-PDF in the cloud cover scheme is:

$$2\Delta q = 2\gamma q_\mathrm{s} = 2\cdot(1 - \mathrm{RH}_\mathrm{crit})q_\mathrm{s}. \tag{3}$$

Dividing Eq. (3) by q_s yields the width of the corresponding RH-PDF. For cloud-free grid-boxes this RH-PDF is equivalent to the RH_cls-PDF. In this case, its which width is

$$2\Delta\mathrm{RH}_\mathrm{cls} = 2\frac{\Delta q}{q_\mathrm{s}} = 2\cdot(1 - \mathrm{RH}_\mathrm{crit}). \tag{4}$$

$\mathrm{RH}_\mathrm{crit}$ is computed by Eq. (2) with values for $c_s = 0.9$, $c_t = 0.7$ and $n_\mathrm{x} = 4$ as used in the cloud cover scheme (Stevens et al., 2013). However, when fractional cloud cover is present $\Delta\mathrm{RH}_\mathrm{cls}$ has to be adjusted to

$$\Delta\mathrm{RH}_\mathrm{cls} = \frac{q_\mathrm{s} - q_\mathrm{cls}}{q_\mathrm{s}} = 1 - \overline{\mathrm{RH}}_\mathrm{cls} \tag{5}$$

so that the variation of RH_cls occurs in the subsaturated part of the cloud cover PDF (see Fig. 1a).

Afterwards, instead of using $\overline{\mathrm{RH}}_\mathrm{cls}$ as input for the calculation of the gf, a stochastic value for clear-sky relative humidity $\mathrm{RH}_\mathrm{cls,new}$ from the inversion of the cumulative distribution function (CDF) is drawn (see Fig. 1b). For this, a random number

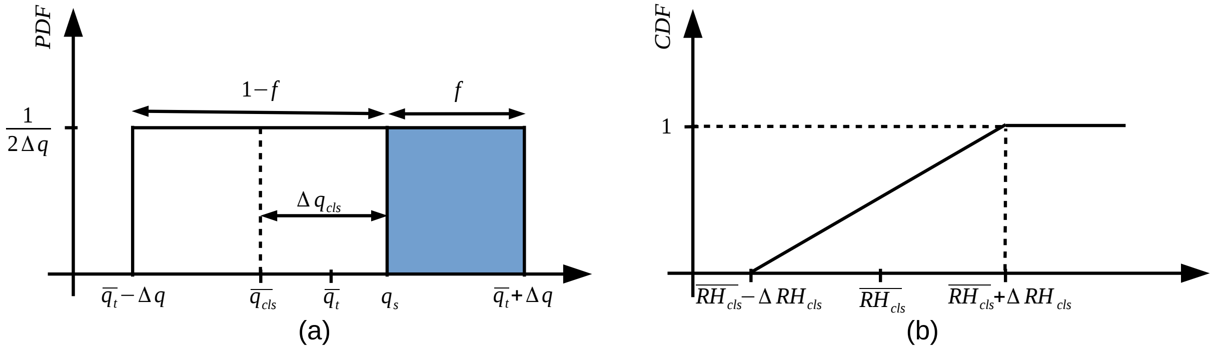

Figure 1. (a) Scheme for predicting fractional cloud cover f with a uniform PDF for the total-water q_t. The blue area indicates the fraction of a grid cell which is covered by clouds. $\Delta\mathrm{RH_{cls}}$ is set to $\Delta q/q_s = 1 - \mathrm{RH_{crit}}$ for a PDF around $\overline{\mathrm{RH}}_\mathrm{cls}$ if no fractional cloud cover is present (not depicted) or set to $(q_\mathrm{s} - q_\mathrm{cls})/q_\mathrm{s} = 1 - \overline{\mathrm{RH}}_\mathrm{cls}$ if fractional cloud cover is present (in the figure shown in terms of specific humidity). (b) Cumulative distribution function (CDF) for a uniform PDF around $\overline{\mathrm{RH}}_\mathrm{cls}$. By the inversion of the CDF and with a random number $a \in [0,1]$ (see Eq. (6)), a value between $\mathrm{RH_{cls}} - \Delta\mathrm{RH_{cls}}$ and $\mathrm{RH_{cls}} + \Delta\mathrm{RH_{cls}}$ is sampled and used as the argument for the hygroscopic growth.

$a \in [0,1]$ is generated and inserted into the following equation:

$$\mathrm{RH_{cls,new}} = \mathrm{RH_{cls,old}} + \Delta\mathrm{RH_{cls}}(2a-1). \tag{6}$$

2.3 Model settings and postprocessing

ECHAM-HAM2 is run with a resolution of T63L31. For aerosol emissions, the AEROCOM II data for 1850 for pre-industrial (PI) and for 2000 for present-day (PD) simulations are used (Lamarque et al. (2010); see section 7). Climatological sea surface temperature (SST) and sea ice distributions are prescribed. Ten-year model free-running (no nudging) simulations starting 1 January 2000 are performed with PI and PD aerosol emissions, both with and without the new parameterization.

The ERFari$_\mathrm{cls}$ is computed by the difference of the global mean net radiative balance under clear-sky conditions between the PD and the PI simulations.

$$\mathrm{ERFari_{cls}} = (SW_\mathrm{net,cls} + LW_\mathrm{net,cls})_{PD} - (SW_\mathrm{net,cls} + LW_\mathrm{net,cls})_{PI} \tag{7}$$

In reality, clouds would mask part of this clear-sky ERF. Therefore, it should be considered as an idealised value. To depict changes in hygroscopic growth we define the squared ratio

$$\beta = \left(\frac{gf_\mathrm{stoch}}{gf_\mathrm{control}}\right)^2 \tag{8}$$

where gf_stoch and gf_control account for the growth factor in the model run with the stochastic parameterization and the control model run, respectively. The squared ratio scales with the effective extinction cross section and therefore describes the influence on aerosol optical depth (AOD).

Satellite retrievals of AOD from the MODerate Resolution Imaging Spectroradiometer (MODIS) platform Aqua (Levy et al., 2013) from the period between August 2002 and December 2010 are used to evaluate the results of implementing subgrid-scale variability of $\mathrm{RH_{cls}}$ into the model. The temporal mean values of AOD measurements ($\overline{\mathrm{AOD}}_{\mathrm{MODIS}}$) for the entire time span (08/2002 - 12/2010) are compared to the temporal means (01/2000 - 12/2009) of the model data ($\overline{\mathrm{AOD}}_{\mathrm{control}}$, $\overline{\mathrm{AOD}}_{\mathrm{stoch}}$). However, differences between the model AOD with and without the new parameterization are small compared to differences between the AOD of both model runs and the AOD measured by MODIS-Aqua. In order to estimate if subgrid-scale variability improves the model performance on AOD we assess the change in absolute differences

$$c = |\overline{\mathrm{AOD}}_{\mathrm{stoch}} - \overline{\mathrm{AOD}}_{\mathrm{MODIS}}| - |\overline{\mathrm{AOD}}_{\mathrm{control}} - \overline{\mathrm{AOD}}_{\mathrm{MODIS}}|. \tag{9}$$

A value of c less than 0 implies that the implementation of subgrid-scale variability of $\mathrm{RH_{cls}}$ has improved the model skill to simulate AOD.

3 Results

In the following results from PD simulations, if not specified differently, are presented. In Figure 2a the global mean profiles of β are shown for each aerosol mode. Hygroscopic growth of aerosols is in general enhanced due to the implementation of a subgrid-scale variability of $\mathrm{RH_{cls}}$. We find that the effect is stronger for aerosol particles with a large particle radius. Thus, the effect is stronger for particles from CS and AS mode than for particles from KS and NS mode. Moreover, the effect on hygroscopic growth has a maximum between 700 hPa and 600 hPa for each aerosol mode.

The global mean AOD increases by 0.009 ± 0.002 ($\sim 7.8\,\%$). The response in AOD is weaker in simulations with PI emissions with a global mean difference of 0.006 ± 0.002 ($\sim 6.0\,\%$). Here, uncertainties are computed for a 95 %-confidence interval on basis of yearly mean values from the temporal variability. In differences, uncertainties are added in quadrature. Figure 3a shows that, as expected, the AOD increased especially in lower latitudes with a mean of about 0.013 in the tropics. Furthermore, the figure reveals that the AOD of diagnosed aerosol water (WAT) dominates the change in total AOD, not the change in dry matter of SS or SO4. Figure 3b shows the zonal mean AOD values from the model runs with and without the stochastic parameterization and from satellite measurements of MODIS-Aqua. Changes due to the new parameterization are small in comparison to the general difference between modelled and measured AOD. The implementation of the subgrid-scale variability improves ($c < 0$) the model performance especially over land and areas with high anthropogenic emissions like East China and the East Coast of the United States. In contrast, model performance is worse ($c > 0$) over the Northern Atlantic Ocean, the Pacific around Hawaii and over most parts of the oceans in the southern hemisphere (not depicted). The global mean value of c is -0.001. This implies that the implemented parameterization has just a very small positive influence on modelled AOD ($\overline{\mathrm{AOD}}_{\mathrm{model}} \simeq 0.12$) with respect to AOD measurements from MODIS-Aqua.

Furthermore, the implementation of the new parameterization enhanced the ratio of scattering efficiency to total extinction efficiency, ω, for the CS, AS and KS aerosol mode with a maximum for the KS mode ($2.6\,\%$). Therefore, more extinction occurs due to scattering. The effective extinction cross section, σ, increases for the CS, AS and KS aerosol mode as well. The strongest change is visible for the KS mode with a change by 15.1 %. Note that no output for ω and σ is generated by the model for NS mode. Finally, the Ångström exponent α changes by -0.8 $\cdot 10^{-3} \pm 11 \cdot 10^{-3}$. This confirms that particles are on average bigger in the model run with the stochastic parameterization than in the control model run.

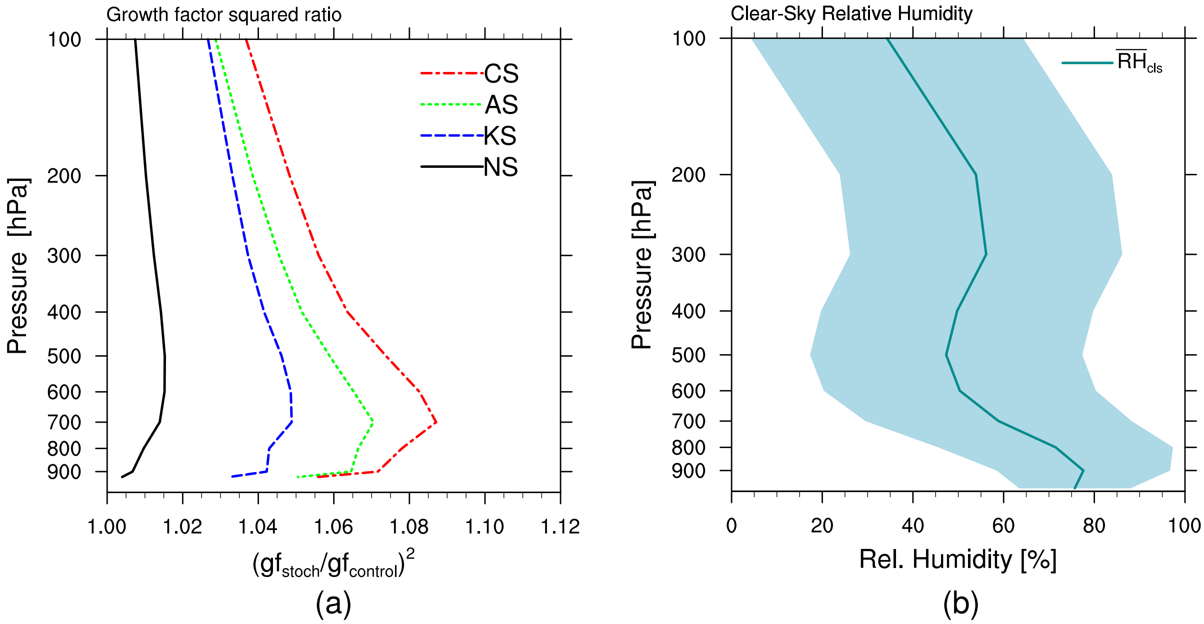

Figure 2. (a) Profile of the global mean of β, the squared ratio of the growth factor between the run with the stochastic parameterization of hygroscopic growth gf_{stoch} and the control run gf_{control}. CS is the soluble Coarse aerosol mode ($r > 0.5\,\mu$m). AS the soluble Accumulation ($0.05 < r < 0.5\,\mu$m), KS the soluble Aitken ($0.005 < r < 0.05\,\mu$m) and NS the soluble Nucleation aerosol mode ($r < 0.005\,\mu$m). (b) Profile of global mean clear-sky relative humidity (dark blue line) with its corresponding range of subgrid-scale variability (light blue area).

In the following, solar and thermal clear-sky radiation represent the idealised solar and thermal irradiance that would arise from an atmosphere where clouds are absent, whereas all-sky stands for the irradiance that takes the effect of clouds into account. The net clear-sky solar radiation $SW_{\text{net,cls}}$ decreases by $-0.22 \pm 0.07\,\text{W}\,\text{m}^{-2}$. In addition, the net all-sky solar radiation SW_{net} changes by $-0.34 \pm 0.22\,\text{W}\,\text{m}^{-2}$. For PI emissions, the effect on $SW_{\text{net,cls}}$ is with a change of $-0.13 \pm 0.06\,\text{W}\,\text{m}^{-2}$, as anticipated, smaller than for PD emissions. In contrast, a stronger effect in PI runs than in PD runs is visible for SW_{net} ($-0.47 \pm 0.19\,\text{W}\,\text{m}^{-2}$). Responses in the thermal radiation (positive downward) are small. The clear-sky thermal radiation $LW_{\text{net,cls}}$ has a slight positive tendency with a mean value of $0.04 \pm 0.09\,\text{W}\,\text{m}^{-2}$. Similar to solar radiation, the all-sky thermal radiation LW_{net} changes more than the clear-sky radiation with a global mean of $0.06 \pm 0.14\,\text{W}\,\text{m}^{-2}$.

The comparison of ten-year model runs with PD and PI aerosol emissions reveals a change of the $\text{ERFari}_{\text{cls}}$ from $-0.29 \pm 0.09\,\text{W}\,\text{m}^{-2}$ to $-0.45 \pm 0.11\,\text{W}\,\text{m}^{-2}$ ($57\,\%$) in runs without to runs with the new parameterization, respectively. This implies that subgrid-scale variability of RH_{cls} enhances the cooling effect of anthropogenic aerosol emissions by aerosol-radiation interactions in climate simulations. It is interesting to note that the $\text{ERFari}_{\text{cls}}$ increases substantially given the relatively small impact of the revision on present-day TOA balance. This can be attributed to the fact that anthropogenic aerosol is disproportionally hygroscopic. Furthermore, the effect on $\text{ERFari}_{\text{cls}}$ translates into the ERF of anthropogenic aerosols (ERFaer) that has as well a negative tendency (-0.07 ± 0.27). The total cloud cover decreased by $-0.08 \pm 0.14\%$ in PD simulations. In contrast,

Table 1. Changes of global mean values of optical and radiative variables due to the implementation of subgrid-scale variability of $\mathrm{RH_{cls}}$ are listed. Uncertainties of the mean value are calculated for a 95 %-confidence interval on basis of yearly mean values from the temporal variability. Uncertainties of differences are added in quadrature. ω is the ratio of the scattering efficiency to the total extinction efficiency and σ the effective extinction cross section. The indices KS, AS and CS stand for Aitken, Accumulation and Coarse mode. α is the Ångström exponent, SW_{net} the net short wave radiation and with index $SW_{\mathrm{net,cls}}$ the net short wave radiation in the clear-sky part. With the same meaning for the indices LW is the longwave radiation. TCC is the total cloud cover. Results are presented for present-day and pre-industrial emissions.

Variable	Stoch	Control	Difference	Relative deviation
$\mathrm{ERFari_{cls}}$ [$\mathrm{W\,m^{-2}}$]	-0.45 ± 0.11	-0.29 ± 0.09	-0.16 ± 0.14	57%
ERFaer [$\mathrm{W\,m^{-2}}$]	-1.52 ± 0.16	-1.45 ± 0.21	-0.07 ± 0.27	5%

	Present-Day		Pre-Industrial	
Variable	Difference	Relative deviation	Difference	Relative deviation
SW_{net} [$\mathrm{W\,m^{-2}}$]	-0.34 ± 0.22	$-0.15\,\%$	-0.47 ± 0.19	$-0.20\,\%$
$SW_{\mathrm{net,cls}}$ [$\mathrm{W\,m^{-2}}$]	-0.22 ± 0.07	$-0.08\,\%$	-0.13 ± 0.06	$-0.05\,\%$
LW_{net} [$\mathrm{W\,m^{-2}}$]	0.06 ± 0.14	$0.03\,\%$	0.26 ± 0.17	$0.10\,\%$
$LW_{\mathrm{net,cls}}$ [$\mathrm{W\,m^{-2}}$]	0.04 ± 0.09	$0.02\,\%$	0.11 ± 0.10	$0.04\,\%$
TCC [%]	-0.08 ± 0.14	$-0.13\,\%$	0.17 ± 0.14	$0.26\,\%$
AOD	0.009 ± 0.002	$7.8\,\%$	0.006 ± 0.002	$6.0\,\%$
ω_{KS}	0.015 ± 0.003	$2.64\,\%$	0.014 ± 0.005	$2.42\,\%$
ω_{AS}	$(1.1 \pm 0.4) \cdot 10^{-3}$	$0.11\,\%$	$(0.9 \pm 0.6) \cdot 10^{-3}$	$0.10\,\%$
ω_{CS}	$(0.03 \pm 0.05) \cdot 10^{-3}$	$0.003\,\%$	$(0.05 \pm 0.15) \cdot 10^{-3}$	$0.005\,\%$
σ_{KS}	$(9.7 \pm 1.0) \cdot 10^{-18}$	$15.1\,\%$	$(8.0 \pm 1.1) \cdot 10^{-18}$	$14.3\,\%$
σ_{AS}	$(20.8 \pm 6.9) \cdot 10^{-15}$	$4.5\,\%$	$(22.7 \pm 7.2) \cdot 10^{-15}$	$4.8\,\%$
σ_{CS}	$(0.69 \pm 0.07 \cdot 10^{-12}$	$3.9\,\%$	$(0.71 \pm 0.07) \cdot 10^{-12}$	$4.0\,\%$
α	$(-0.8 \pm 11.5) \cdot 10^{-3}$	$-0.11\,\%$	$(6.4 \pm 13.8) \cdot 10^{-3}$	$0.94\,\%$

it increased by 0.17 ± 0.14 in PI simulations. The global mean profile of cloud cover f in Fig. 4 reveals a slight increase of cloud cover between 700 and 900 hPa for PD simulations, whereas it mainly decreased below and above this layer. However, in PI runs f increased for most parts of the atmosphere with a very little decrease at around 600 hPa. A summary of the influence of subgrid-scale variability of $\mathrm{RH_{cls}}$ on optical and radiative variables is given in Table 1.

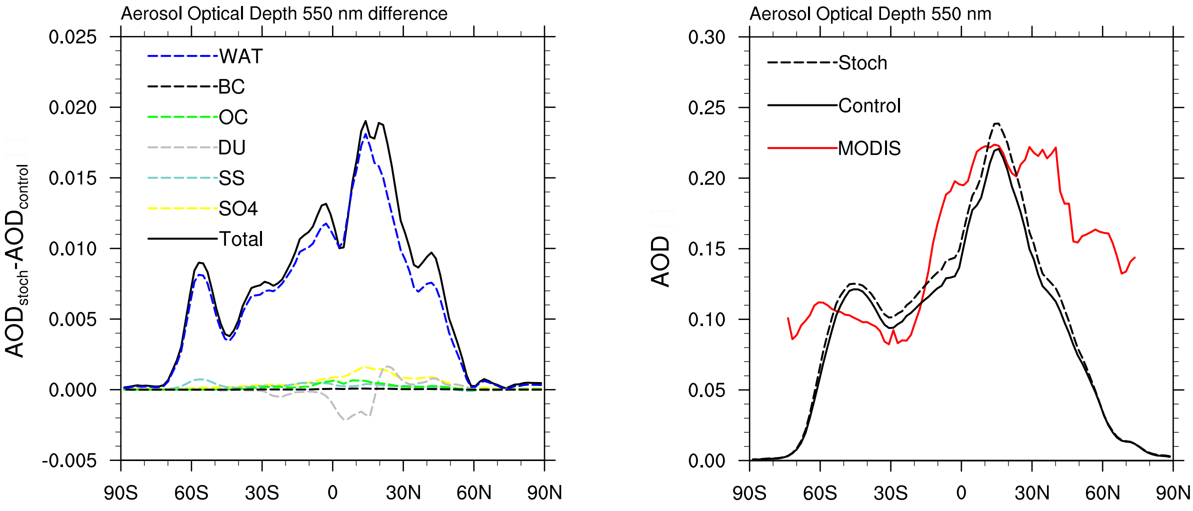

(a) (b)

Figure 3. (a) Difference in AOD between the stochastic variation and the control run in AOD for different aerosol constituents. AOD from diagnosed aerosol water (WAT) dominates the changes. (b) Temporally and zonally averaged clear-sky AOD (computed from on monthly mean values) from the control (plain) and stochastic (dashed) model runs (black, 01/2000 - 12/2009) and MODerate Resolution Imaging Spectroradiometer (Levy et al., 2013) Aqua satellite data (red, 08/2002 - 12/2010) is shown. Two discrepancies arise, namely (i) the fact that the model diagnoses clear-sky AOD also in overcast grid cells, with a relative humidity of RH=1 in these cases, which are dismissed in the MODIS retrieval, and (ii) the point that MODIS uses a conservative cloud masking, i.e. excludes pixels near cloud edges, whereas the model uses all clear-sky pixels.

4 Discussion

As for the previous section, we discuss in the following the results from PD simulations, if not specified differently. In model runs with the new parameterization aerosol particles swell stronger at each height level due to the non-linear nature of hygroscopic growth (see Eq. 1). The positive curvature of this function for $\mathrm{RH_{cls}} \in [0,1]$ implies that by applying a uniform PDF on $\mathrm{RH_{cls}}$ the expected value of $gf(\mathrm{RH_{cls}})$ is greater than $gf(\overline{\mathrm{RH}}_{\mathrm{cls}})$ with $\overline{\mathrm{RH}}_{\mathrm{cls}}$ being the grid box mean clear-sky relative humidity.

Effects are stronger for aerosol particles with a larger radius, and thus, particles from CS and AS mode. Three reasons can explain the vertical shape of the gf-profiles:

(1) Clear-sky relative humidity has a decreasing trend with height in the model (see Fig. 2b). The same change of $\mathrm{RH_{cls}}$ in a drier environment leads to a smaller change in gf than in a more humid environment (unless saturation is reached) because of the non-linearity of Eq. (1) and therefore leads to smaller slopes of $gf(\mathrm{RH})$ in the drier environment.

(2) Very hygroscopic aerosol particles are more sensitive to changes in relative humidity and larger particles tend to become deposited by impaction and sedimentation more easily. The main hygroscopic aerosol types are sulphate and sea salt, where sea salt ($\kappa = 1.12$) is more hygroscopic than sulphate ($\kappa = 0.6$). Sea salt particles are emitted at the surface of the ocean. Due to

their high κ value, sea salt particles grow strongly, are deposited easily and can not reach high altitudes. Therefore, the aerosol composition of the atmosphere shifts towards less hygroscopic components (smaller κ values) with height and the effect of perturbing relative humidity on hygroscopic growth becomes weaker with smaller κ values. Pringle et al. (2010) examined the global distribution of κ and found that especially at marine sites κ-values decrease with height, whereas at continental sites κ tends to be more constant with height. However, (1) and (2) can only explain a decreasing trend of β with height but not the maxima of the β profiles between 600 and 700 hPa.

(3) The critical relative humidity determines the width of the PDF which is used to vary $\mathrm{RH_{cls}}$ stochastically. The width $2\Delta\mathrm{RH_{cls}}$ of the PDF is calculated by $\Delta\mathrm{RH_{cls}} = 1 - \mathrm{RH}_{crit}$ as described in section 2. But RH_{crit} is a function of height (see Eq. (2)). It decreases from the surface to 600 hPa from 0.9 to close to 0.7. For higher altitudes, it is nearly constant and just converges slowly towards 0.7 (see Fig. 2b). This in fact means that the width of the PDF increases with height from the surface to 600 hPa. Then, it is almost constant. The positive curvature of Eq. (Equation 1) implies that mean hygroscopic growth is stronger the wider the PDF is. The increasing width of the PDF explains why β becomes greater with height until 600 hPa. Above, the two other effects are dominant and β decreases again.

The AOD, the effective extinction cross section, σ, and the ratio of scattering efficiency to total extinction efficiency, ω, are enhanced because of the increase in the geometrical radius of the particles. Anthropogenic aerosols that arise in PD simulations are disproportionally hygroscopic. Therefore, hygroscopic aerosols swell stronger due to the new parameterization in PD than in PI simulations and scatter more solar radiation. This leads in turn to a higher AOD in PD than PI runs. As Figure 3b demonstrates, little can be said about improved skill of ECHAM-HAM2 to model AOD in respect to AOD satellite retrievals of MODIS-Aqua. However, there is a hint at a slight improvement especially over land when including the subgrid-scale variability of $\mathrm{RH_{cls}}$.

The net clear-sky solar radiation $SW_{\mathrm{net,cls}}$ decreases ($\Delta SW_{\mathrm{net,cls}} = -0.22\,\mathrm{W\,m^{-2}}$) due to an increased reflection of solar radiation as indicated by an increased ω. However, the effect on the net all-sky solar radiation SW_{net} is greater ($\Delta SW_{\mathrm{net}} = -0.34\,\mathrm{W\,m^{-2}}$) than the effect on the net clear-sky solar radiation. This is maybe due to the fact that although total cloud cover (TCC) decreased by -0.08%, cloud cover in is slightly enhanced in height levels between about 700 and 900 hPa (see graph for PD in Fig. 4). Hence, more solar radiation is reflected back to space by these clouds.

We proceed with the discussion of differences that arise between PD and PI simulations. The change in $SW_{\mathrm{net,cls}}$ is stronger for PD than for PI emissions because backscattering of solar radiation is more enhanced by the new parameterization in PD than in PI simulations as already explained. Because effects on $LW_{\mathrm{net,cls}}$ are in general small, this translates as well into a strong response in $\mathrm{ERFari_{cls}}$. In contrast, the response in SW_{net} was greater in PI runs ($\Delta SW_{\mathrm{net,PI}} = -0.47\,\mathrm{W\,m^{-2}}$) than in PD runs ($\Delta SW_{\mathrm{net,PD}} = -0.34\,\mathrm{W\,m^{-2}}$). We assume that this might be due to the enhanced total cloud cover in the PI simulations ($\Delta TCC_{\mathrm{PI}} = 0.17$) whereas total cloud cover decreased in PD simulations ($\Delta TCC_{\mathrm{PD}} = -0.08$). However, cloud cover between 700 and 900 hPa increased stronger in PD than in PI simulations (see Fig. 4). This slightly weakens the hypothesis that clouds caused a stronger decrease in SW_{net} in PI than in PD simulations, since low-level clouds are known to have a cooling effect on the radiative balance of the Earth (Hartmann et al., 1992; Chen et al., 2000).

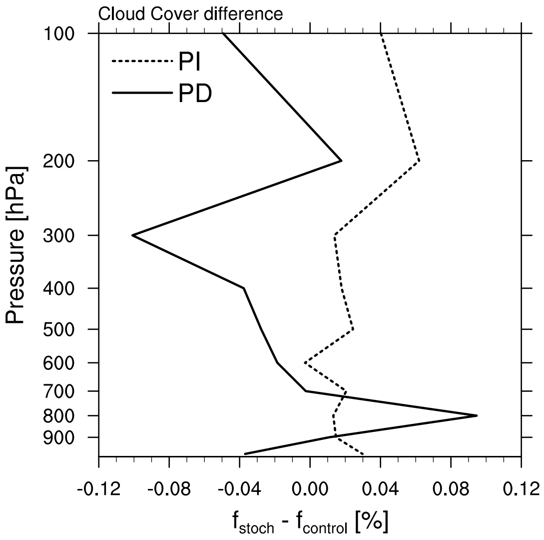

Figure 4. Difference in cloud cover f due to the implementation of subgrid-scale variability of $\mathrm{RH}_{\mathrm{cls}}$ for PI (dashed) and PD (solid) simulations.

The stronger increase in cloud cover for the higher troposphere in PI simulations (see Fig. 4) might explain the strong response LW_{net} in PI simulations ($\Delta LW_{\mathrm{net,PI}} = 0.26\,\mathrm{W\,m^{-2}}$). High-thin clouds, namely Cirrus clouds, are known to have positive effect on outgoing longwave radiation (Hartmann et al., 1992; Chen et al., 2000).

5 Conclusions

This study investigated the effect of implementing a stochastic parameterization for subgrid-scale variability of clear-sky relative humidity $\mathrm{RH}_{\mathrm{cls}}$ on hygroscopic growth of aerosol particles as well as the subsequent changes of optical properties of the atmosphere and the radiative balance of the Earth. The implementation of the new parameterization led to stronger swelling of aerosol particles (as expected) and therefore increased the AOD ($\sim 7.8\,\%$). Furthermore, the increased AOD caused stronger backscattering of solar radiation under clear-sky conditions $SW_{\mathrm{net,cls}}$ ($-0.08\,\%$). Most importantly, the revision had a very strong influence on the simulated effective radiative forcing due to aerosol-radiation interaction under clear-sky conditions $\mathrm{ERFari}_{\mathrm{cls}}$ ($57\,\%$). In earlier studies RFari by sulphate increased in GCMs by about 10% when an idealized distributions for RH was implemented (Haywood and Shine, 1997; Haywood and Ramaswamy, 1998). Further studies found that GCMs underestimate RFari of sulphate when subgrid-scale variability of RH is not taken into account by 73 % in a limited-area-model case study (Haywood et al., 1997), by 30 to 80 % in a study that used a cloud-resolving model over a tropical ocean and a mid-latitude continental region (Petch, 2001) and by 30 to 40 % in a regional study (Europe and much of the North Atlantic) with a high resolution model (Myhre et al., 2002).

The comparison with satellite data reveals that the new parameterization performs better in areas where sulphate is the dominant soluble aerosol type. This is especially the case over land and in areas with high anthropogenic aerosol (precursor) emissions. In contrast, model performance is worse where sea salt is the main aerosol types. This occurs maybe due to the fact that sea salt fluxes are still not represented well enough in ECHAM6-HAM2. One might be able to further improve the parameterization of subgrid-scale variability of $\mathrm{RH_{cls}}$ by applying the subsaturated part of the β-function from the optional Tompkins (2002) cloud cover scheme that prognostically treats the total-water variability PDF. Furthermore, Figure 2 in Quaas (2012) indicates that the critical relative humidity, $\mathrm{RH}_{\mathtt{crit}}$, that defines the width of the introduced $\mathrm{RH_{cls}}$-PDF, varies horizontally in the same scale as vertically. Therefore, the width of the $\mathrm{RH_{cls}}$-PDF could be extended from just height dependent to height and zonal or even height, zonal and meridional dependent.

6 Code availability

The changed model code is available upon request from the first author.

7 Data availability

The ECHAM6-HAM2 model output data used in this study is archived at the Leipzig Institute for Meteorology and is available upon request from the authors. Satellite data from MODIS-Aqua can be obtained at https://neo.sci.gsfc.nasa.gov/. AEROCOM emission data can be downloaded at http://aerocom.met.no/emissions.html.

Acknowledgements. The ECHAM-HAM model is developed by a consortium composed of ETH Zurich, Max Planck Institut für Meteorologie, Forschungszentrum Jülich, University of Oxford, the Finnish Meteorological Institute and the Leibniz Institute for Tropospheric Research, and managed by the Center for Climate Systems Modeling (C2SM) at ETH Zurich. The MODIS data are from the NASA Goddard Space Flight Center (ftp://laadsweb.nascom.nasa.gov). The CERES data were obtained from the Atmospheric Sciences Data Center at NASA Langley Research Center (http://ceres.larc.nasa.gov). Funding by the European Research Council in Starting Grant, grant agreement FP7-306284 (QUAERERE) is acknowledged.

References

Beer, A.: Bestimmung der Absorption des rothen Lichts in farbigen Flüssigkeiten, Annalen der Physik, 162, 78–88, 1852.

Boucher, O., Randall, D., Artaxo, P., Bretherton, C., Feingold, G., Forster, P., Kerminen, V.-M., Kondo, Y., Liao, H., Lohmann, U., et al.: Clouds and aerosols, in: Climate change 2013: The physical science basis. Contribution of working group I to the fifth assessment report of the intergovernmental panel on climate change, pp. 571–657, Cambridge University Press, 2013.

Chen, T., Rossow, W. B., and Zhang, Y.: Radiative Effects of Cloud-Type Variations, J. Climate, 13, 264–286, doi:10.1175/1520-0442(2000)013<0264:REOCTV>2.0.CO;2, 2000.

Donner, L. J., Wyman, B. L., Hemler, R. S., Horowitz, L. W., Ming, Y., Zhao, M., Golaz, J.-C., Ginoux, P., Lin, S.-J., Schwarzkopf, D. M., Austin, J., Alaka, G., Cooke, W. F., Delworth, T. L., Freidenreich, S. M., Gordon, C. T., Griffies, S. M., Held, I. M., Hurlin, W. J., Klein, S. A., Knutson, T. R., Langenhorst, A. R., Lee, H.-C., Lin, Y., Magi, B. I., Malyshev, S. L., Milly, P. C. D., Naik, V., Nath, M. J., Pincus, R., Ploshay, J. J., Ramaswamy, V., Seman, C. J., Shevliakova, E., Sirutis, J. J., Stern, W. F., Stouffer, R. J., Wilson, R. J., Winton, M., Wittenberg, A. T., and Zeng, F.: The dynamical core, physical parameterizations, and basic simulation characteristics of the atmospheric component AM3 of the GFDL global coupled model CM3, 24, 3484–3519, doi:10.1175/2011JCLI3955.1, 2011.

Ghan, S. J., Leung, L. R., Easter, R. C., and Abdul-Razzak, H.: Prediction of cloud droplet number in a general circulation model, J. Geophys. Res., 102, 21 777–21 794, 1997.

Ginoux, P.: Atmospheric chemistry: Warming or cooling dust?, Nature Geosci, 10, 246–248, doi:10.1038/ngeo2923, 2017.

Golaz, J.-C., Salzmann, M., Donner, L. J., Horowitz, L. W., Ming, Y., and Zhao, M.: Sensitivity of the aerosol indirect effect to subgrid variability in the cloud parameterization of the GFDL Atmosphere General Circulation Model AM3, J. Clim., 24, doi:10.1175/2010JCLI3945.1, 2011.

Gustafson, W. I., Qian, Y., and Fast, J. D.: Downscaling aerosols and the impact of neglected subgrid processes on direct aerosol radiative forcing for a representative global climate model grid spacing, J. Geophys. Res., 116, D13 303, doi:10.1029/2010JD015480, 2011.

Haarig, M., Ansmann, A., Gasteiger, J., Kandler, K., Althausen, D., Baars, H., and Farrell, D. A.: Dry versus wet marine particle optical properties: RH dependence of depolarization ratio, backscatter and extinction from multiwavelength lidar measurements during SALTRACE, Atmos. Chem. Phys. Discuss., 2017, 1–32, doi:10.5194/acp-2017-545, 2017.

Hartmann, D. L., Ockert-Bell, M. E., and Michelsen, M. L.: The Effect of Cloud Type on Earth's Energy Balance: Global Analysis, J. Climate, 5, 1281–1304, doi:10.1175/1520-0442(1992)005<1281:TEOCTO>2.0.CO;2, 1992.

Haywood, J. M. and Ramaswamy, V.: Global sensitivity studies of the direct radiative forcing due to anthropogenic sulfate and black carbon aerosols, J. Geophys. Res., 103, 6043–6058, doi:10.1029/97JD03426, 1998.

Haywood, J. M. and Shine, K. P.: Multi-spectral calculations of the direct radiative forcing of tropospheric sulphate and soot aerosols using a column model, Q.J.R. Meteorol. Soc., 123, 1907–1930, doi:10.1002/qj.49712354307, 1997.

Haywood, J. M., Ramaswamy, V., and Donner, L. J.: A limited-area-model case study of the effects of sub-grid scale Variations in relative humidity and cloud upon the direct radiative forcing of sulfate aerosol, Geophys. Res. Lett., 24, 143–146, doi:10.1029/96GL03812, 1997.

Köhler, H.: The nucleus in and the growth of hygroscopic droplets, Trans. Faraday Soc., 32, 1152–1161, doi:10.1039/TF9363201152, 1936.

Lamarque, J.-F., Bond, T. C., Eyring, V., Granier, C., Heil, A., Klimont, Z., Lee, D., Liousse, C., Mieville, A., Owen, B., et al.: Historical (1850–2000) gridded anthropogenic and biomass burning emissions of reactive gases and aerosols: methodology and application, Atmospheric Chemistry and Physics, 10, 7017–7039, 2010.

Lambert, J. H.: Photometria, sive de Mensura et Gradibus Luminis, Colorum et Umbrae, VE Klett Augustae Vindelicorum, 1760.

Levy, R. C., Mattoo, S., Munchak, L. A., Remer, L. A., Sayer, A. M., Patadia, F., and Hsu, N. C.: The Collection 6 MODIS aerosol products over land and ocean, Atmos. Meas. Tech., 6, 2989–3034, doi:10.5194/amt-6-2989-2013, 2013.

Lohmann, U., Stier, P., Hoose, C., Ferrachat, S., Kloster, S., Roeckner, E., and Zhang, J.: Cloud microphysics and aerosol indirect effects in the global climate model ECHAM5-HAM, 7, 3425–3446, 2007.

Mie, G.: Beiträge zur Optik trüber Medien, speziell kolloidaler Metallösungen, Annalen der physik, 330, 377–445, 1908.

Myhre, G., Jonson, J. E., Bartnicki, J., Stordal, F., and Shine, K. P.: Role of spatial and temporal variations in the computation of radiative forcing due to sulphate aerosols: A regional study, Q.J.R. Meteorol. Soc., 128, 973–989, doi:10.1256/003590002321643610, 2002.

Petch, J. C.: Using a cloud-resolving model to study the effects of subgrid-scale variations in relative humidity on direct sulphate-aerosol forcing, Q.J.R. Meteorol. Soc., 127, 2385–2394, doi:10.1002/qj.49712757710, 2001.

Petters, M. D. and Kreidenweis, S. M.: A single parameter representation of hygroscopic growth and cloud condensation nucleus activity, Atmos. Chem. Phys., 7, 1961–1971, doi:10.5194/acp-7-1961-2007, 2007.

Pringle, K. J., Tost, H., Pozzer, A., Pöschl, U., and Lelieveld, J.: Global distribution of the effective aerosol hygroscopicity parameter for CCN activation, Atmos. Chem. Phys., 10, 5241–5255, doi:10.5194/acp-10-5241-2010, 2010.

Quaas, J.: Evaluating the "critical relative humidity" as a measure of subgrid-scale variability of humidity in general circulation model cloud cover parameterizations using satellite data, J. Geophys. Res., 117, D09 208, doi:10.1029/2012JD017495, 2012.

Rosch, J., Heus, T., Brueck, M., Salzmann, M., Mülmenstädt, J., Schlemmer, L., and Quaas, J.: Analysis of diagnostic climate model cloud parametrizations using large-eddy simulations, Q.J.R. Meteorol. Soc., 141, 2199–2205, doi:10.1002/qj.2515, 2015.

Skupin, A., Ansmann, A., Engelmann, R., Seifert, P., and Müller, T.: Four-year long-path monitoring of ambient aerosol extinction at a central European urban site: dependence on relative humidity, Atmos. Chem. Phys., 16, 1863–1876, doi:10.5194/acp-16-1863-2016, 2016.

Stevens, B., Giorgetta, M., Esch, M., Mauritsen, T., Crueger, T., Rast, S., Salzmann, M., Schmidt, H., Bader, J., Block, K., Brokopf, R., Fast, I., Kinne, S., Kornblueh, L., Lohmann, U., Pincus, R., Reichler, T., and Roeckner, E.: Atmospheric component of the MPI-M Earth System Model: ECHAM6, J. Adv. Model. Earth Syst., 5, 146–172, doi:10.1002/jame.20015, 2013.

Sundqvist, H., Berge, E., and Kristjánsson, J. E.: Condensation and cloud parameterization studies with a mesoscale numerical weather prediction model, Monthly Weather Review, 117, 1641–1657, 1989.

Tiedtke, M.: Representation of clouds in large scale models, Mon. Weather Rev., 121, 3040–3061, 1993.

Tompkins, A. M.: A Prognostic Parameterization for the Subgrid-Scale Variability of Water Vapor and Clouds in Large-Scale Models and Its Use to Diagnose Cloud Cover, J. Atmos. Sci., 59, 1917–1942, doi:10.1175/1520-0469(2002)059<1917:APPFTS>2.0.CO;2, 2002.

Weigum, N., Schutgens, N., and Stier, P.: Effect of aerosol subgrid variability on aerosol optical depth and cloud condensation nuclei: implications for global aerosol modelling, Atmos. Chem. Phys., 16, 13 619–13 639, doi:10.5194/acp-16-13619-2016, 2016.

Zhang, K., O'Donnell, D., Kazil, J., Stier, P., Kinne, S., Lohmann, U., Ferrachat, S., Croft, B., Quaas, J., Wan, H., Rast, S., and Feichter, J.: The global aerosol-climate model ECHAM-HAM, version 2: sensitivity to improvements in process representations, Atmos. Chem. Phys., 12, 8911–8949, doi:10.5194/acp-12-8911-2012, 2012.

Zieger, P., Fierz-Schmidhauser, R., Weingartner, E., and Baltensperger, U.: Effects of relative humidity on aerosol light scattering: results from different European sites, Atmos. Chem. Phys., 13, 10 609–10 631, doi:10.5194/acp-13-10609-2013, 2013.